Spatial and temporal evolution of ionic fragments produced by deep core-level ionization

Oksana Travnikova,[1,2,*] Ji-Cai Liu,[3,†] Ralph Püttner,[4] Kari Jänkälä,[5] Nicolas Sisourat,[1] Tatiana Marchenko,[1,2] Renaud Guillemin,[1,2] Denis Céolin,[2] Maria Novella Piancastelli,[1] Faris Gel'mukhanov,[6,7,8] Marc Simon,[1,2] and Victor Kimberg[6,‡]

[1]*Sorbonne Université, CNRS, Laboratoire de Chimie Physique-Matiére et Rayonnement, F-75005 Paris, France*
[2]*Synchrotron SOLEIL, L'Orme des Merisiers, Saint-Aubin, BP 48, F-91192 Gif-sur-Yvette Cedex, France*
[3]*Department of Mathematics and Physics, North China Electric Power University, 102206 Beijing, China*
[4]*Fachbereich Physik, Freie Universität Berlin, D-14195 Berlin, Germany*
[5]*Nano and Molecular Systems Research Unit, Faculty of Science, University of Oulu, 90014 Oulu, Finland*
[6]*Theoretical Chemistry and Biology, KTH Royal Institute of Technology, 10691 Stockholm, Sweden*
[7]*Federal Siberian Research Clinical Centre under the Federal Medical Biological Agency, 660037 Krasnoyarsk, Russia*
[8]*International Research Center of Spectroscopy and Quantum Chemistry–IRC SQC, Siberian Federal University, 660041 Krasnoyarsk, Russia*

(Received 1 October 2025; accepted 2 January 2026; published 23 January 2026)

Multiply charged molecules fragment under Coulomb repulsion, leaving characteristic fingerprints in ensuing electronic decay. Using K-shell ionization of HCl as a benchmark, we identify metastable intermediates that persist to internuclear separations beyond 100 a.u., where weakened Coulomb interactions enable the emergence of narrow atomic lines, while short-lived states decay at smaller separations, producing broad, red-shifted backgrounds. This work provides a previously missing dynamical description of coupled electronic and nuclear evolution in the Coulomb fragmentation regime.

DOI: 10.1103/6bdq-fwrd

I. INTRODUCTION

Understanding how inner-shell ionization triggers coupled electronic and nuclear dynamics is central to the physics of x-ray-matter interactions. The energy deposited by hard x rays initiates cascades of electronic relaxation that redistribute charge and energy within a molecule on femtosecond timescales, with profound implications for a wide range of radiation-induced processes, including Coulomb explosion [1–6]. Despite their ubiquity, the spectral fingerprints of electronic decay occurring in the presence of evolving Coulomb fields, where charge build-up and nuclear dynamics proceed simultaneously, remain largely unexplored. Addressing this question is particularly timely as gas-phase physics expands into the hard x-ray regime at synchrotron facilities [7–12], allowing controlled single-photon initiation of Auger cascades, and as x-ray free-electron lasers provide access to highly charged, core-ionized molecular systems that undergo sequential relaxation or can be probed during charge redistribution and fragmentation induced by an earlier pulse [13–17]. These developments call for a dynamical description that accounts for how long-range Coulomb interactions shape Auger line profiles and influence nuclear evolution in molecular fragmentation.

Despite extensive studies, mostly in the soft x-ray domain, previous investigations of x-ray-induced coupled electronic and ultrafast nuclear dynamics have primarily focused on systems where the electronic states possess short-range dissociative potential energy curves (PECs), leading to well-understood patterns of broad molecular bands near equilibrium and narrow atomic-like lines as fragments separate [18–27]. In contrast, when long-range interactions between charged fragments cannot be neglected, this conventional picture breaks down. In such cases, as in dissociating molecules with intrinsic Coulomb repulsion, the PECs remain repulsive even at large internuclear distances, preventing fragments from reaching a noninteracting limit. Consequently, the formation of spectral features can differ qualitatively, reflecting the evolution of interfragment potentials throughout the cascade.

In the hard x-ray regime, molecular dynamics during sequential relaxation of an initial deep-inner-shell vacancy can unfold on timescales far longer than those of single-step core-hole decay. Auger cascades thus constitute a qualitatively different regime: intermediate levels are not populated instantaneously but sequentially, and their effective lifetimes are governed not only by their intrinsic (partial) decay rates but also by population transfer from preceding steps [28–30]. As a result, cascade intermediates can persist for hundreds of

*Contact author: oksana.travnikova@sorbonne-universite.fr
†Contact author: jicailiu@ncepu.edu.cn
‡Contact author: kimberg@kth.se

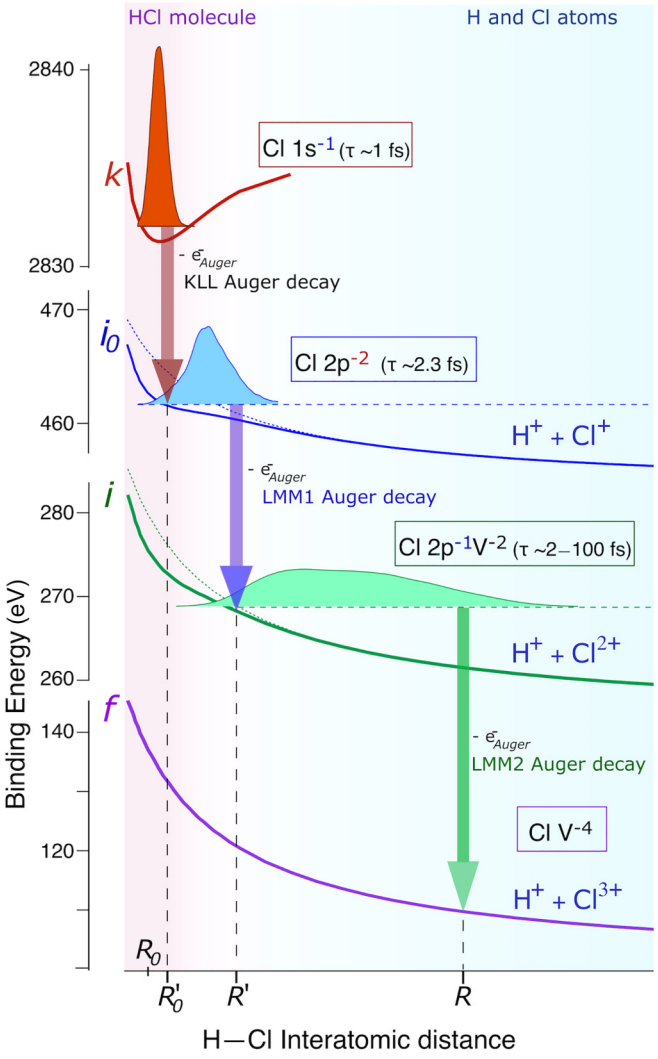

FIG. 1. Scheme of nonresonant Auger cascade for the dominant *KLL* decay path following Cl 1*s* ionization in HCl. PECs for i_0 and i states (solid lines) deviate from model Coulomb potentials (dotted) in the region close to equilibrium R_0, characterized by strong covalent bonding. Beyond this region, PECs of i_0, i, and f states are described as Coulomb potentials $\omega_{i_0}^{(\mathrm{at})} + \frac{1}{R}$, $\omega_i^{(\mathrm{at})} + \frac{2}{R}$, and $\omega_f^{(\mathrm{at})} + \frac{3}{R}$, respectively.

femtoseconds, orders of magnitude longer than typical single-core-hole lifetimes [30–32].

II. PHYSICAL PICTURE

To explore these effects in a minimal testbed, we study the benchmark diatomic HCl after deep-inner-shell (Cl 1*s*) ionization by hard x rays, where charge build-up and evolving Coulomb potentials control the ensuing coupled electron-nuclear dynamics. Cl 1*s* ionization initiates a cascade of Auger decays that progressively fill inner-shell vacancies. The dominant relaxation channel proceeds via a *KLL* transition (Fig. 1), in which the 1*s* hole is filled in the first step, producing two vacancies in the 2*p* shell. These are subsequently filled in two consecutive *LMM* Auger decays (*LMM*1 and *LMM*2):

$$\mathrm{HCl} + \omega(> 2832\ \mathrm{eV}) \rightarrow \mathrm{HCl}^{+}{}_{(1s^{-1})} + \mathrm{e}^{-}_{\mathrm{ph}}$$
$$\xrightarrow{KLL(\tau_0 \approx 1fs)} \mathrm{HCl}^{2+}{}_{(2p^{-2})} + e^{-}_{KLL}$$
$$\xrightarrow{LMM1(\tau_1 \approx 2.3fs)} \mathrm{HCl}^{3+}{}_{(2p^{-1}V^{-2})} + e^{-}_{LMM1}$$
$$\xrightarrow{LMM2(\tau_2 \sim 2...112fs)} \mathrm{HCl}^{4+}{}_{(V^{-4})} + e^{-}_{LMM2},$$

where V denotes a valence orbital and τ the intermediate-state lifetime.

Following the initial *KLL* decay, the system evolves along dissociative PECs, enabling extensive nuclear dynamics and multistep ultrafast dissociation (MUST UFD) [33,34]. These processes occur in both resonant Auger cascades (RAC), triggered by excitation into an unoccupied antibonding orbital, and nonresonant Auger cascades (NAC), initiated above the ionization threshold. In resonant excitation, the excited electron typically remains localized on the hydrogen site [20–27]. The sequential Auger steps then proceed while the hydrogen remains neutral, producing narrow, atomic-like features throughout the cascade decay [33,34]. By contrast, in NAC, initiated by Cl 1*s* ionization above threshold, no spectator electron is present: the hydrogen fragment leaves as H^+, experiencing strong Coulomb repulsion from the multiply charged Cl fragment. As a result, the spectra exhibit broadened and asymmetric features, while narrow atomic lines appear only when decay occurs after very large separations, exceeding 100 a.u. and corresponding to lifetimes of over 100 fs, as demonstrated below.

Experimentally, in the final *LMM*2 step of the cascade triggered by hard x-ray ionization of HCl, the NAC spectrum reveals two prominent features [A_1 and A_2, Fig. 2(a)] superimposed on a broad background. These features appear at the same kinetic energies in both RAC and NAC spectra, suggesting a common origin. In NAC, however, the peaks are broader and exhibit a pronounced low-energy tail [Figs. 2(a) and 2(d)], reflecting fundamental differences in the cascade dynamics that shape the spectral profiles. Here we focus on the NAC channel, whose underlying cascade physics has not been previously explored. We show that distinct signatures on conventional Auger spectra allow to track long-range Coulomb effects. In detail, the line shapes encode the spatial separation and temporal evolution of the dissociating fragments, in agreement with the comprehensive theoretical description of the Auger cascade developed in this work.

III. EXPERIMENTAL METHODS

The experiments were carried out at the GALAXIES beamline [35] of the 2.75-GeV SOLEIL synchrotron using the hard x-ray photoelectron spectroscopy (HAXPES) setup [36]. In brief, linearly polarized x rays were monochromatized by a Si(111) double-crystal and focused into a gas cell. Commercial HCl (Air Liquide, >99% purity) was introduced into the cell, while maintaining constant low pressure in the analysis chamber at about 10^{-5} mbar. Auger electrons were collected by an EW4000 Scienta analyzer equipped with a wide-angle lens, aligned parallel to the polarization vector of the radiation. The estimated electron energy resolution was

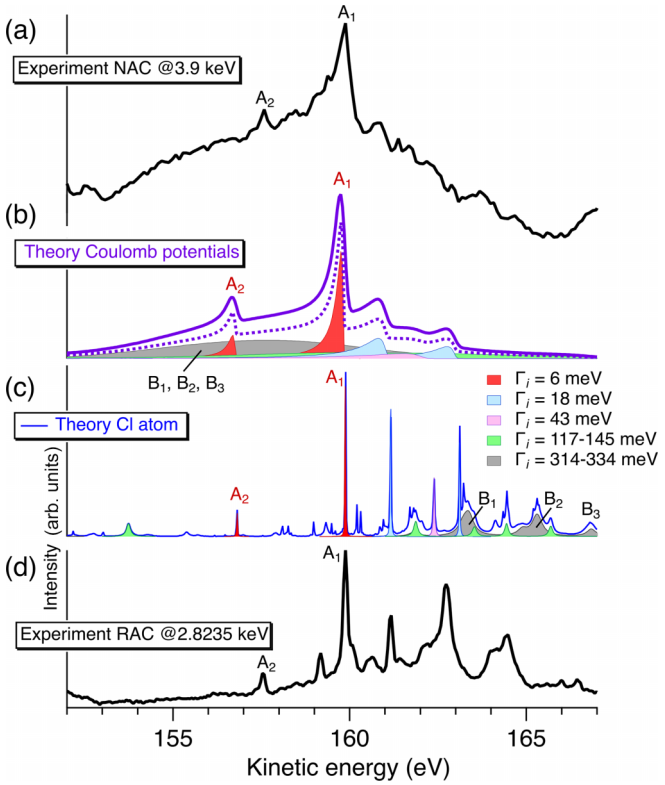

FIG. 2. *LMM*2 Auger spectra of HCl following Cl 1*s* core ionization [NAC, (a), (b)] and Cl $1s \rightarrow \sigma^*$ core excitation [RAC, (d)]. (a), (d) Experimental spectra recorded at 3.9 keV (NAC), and at 2823.5 eV (RAC), respectively. (b) Simulated NAC spectrum using model Coulomb potentials (dotted magenta), and the same spectrum convolved with a 0.2-eV Gaussian (solid). (c) Computed Auger spectrum of an isolated Cl atom: Cl^{2+} $[2p^5(3s3p)^6] \rightarrow Cl^{3+}$ $[(3s3p)^4]$ (see Table I). In (b), (c), filled curves show transitions with an intensity of more than 15% of the most intense transition, grouped by Auger decay widths and summed accordingly: $\Gamma_i = 6$ (red), 18 (blue), 43 (pink), 117 to 145 (green), and 314 to 334 (gray) meV. All theoretical spectra are shifted by −2.5 eV to align the strongest peak A_1 at 159.9 eV.

∼150 meV at a 100-eV pass energy, and the photon bandwidth was ∼250 meV around 3 keV. Spectra were recorded at the Cl $1s \rightarrow \sigma^*$ resonance (∼2823.5 eV) and well above the Cl 1*s* ionization edge (3900 eV), to capture both resonant (RAC) and nonresonant (NAC) decay channels. The kinetic energy scale was calibrated by the Cl $3p^4$ (^1S) atomic line at 177.32 eV [22]. The NAC spectrum, corresponding to the final *LMM*2 Auger decay step, is presented in Fig. 2(a). For reference, Fig. 2(d) shows the RAC spectrum recorded following Cl $1s \rightarrow \sigma^*$ excitation, which was previously discussed in Ref. [33].

IV. THEORETICAL FRAMEWORK

A. Cascade dynamics following Cl 1s ionization

1. Calculations of cascade Auger decay transitions for atomic Cl

The states and Auger transition matrix elements of atomic Cl were calculated using the Flexible Atomic Code (FAC) [37]. FAC is a versatile inherently relativistic atomic structure program, providing solutions of the Dirac equation via multiconfiguration Dirac-Fock-Slater framework (see, e.g., Ref. [38]). In this method, the final atomic-state functions (ASFs) with total angular momentum, projection, and parity are constructed as linear combinations in the basis of configuration state functions (CSFs), which are antisymmetrized angular momentum coupled linear combinations *N*-electron Slater determinants. The relativistic one-electron wave functions in the determinants are obtained in the average energy-level scheme by solving the Dirac-Fock equations.

In the present case the starting point for the Auger decay cascade of Cl* was $1s^12s^22p^63s^23p^6$. It thus mimics the case where the K-shell of HCl atom is ionized and the valence orbital of the molecule is fully localized to the Cl site. Even though in the present work the focus is in the *LMM*2 spectrum of the K-shell cascade to get the intensities of that Auger spectrum correct, all prior Auger decay steps need to be calculated for obtaining the correct initial-state populations. It was also seen that for precise Auger decay predictions, especially in the core-excited Cl^{2+} and Cl^{3+} ionic states, the correlation between 3*s* and 3*d* one-electron orbitals is important. This forced expanding the CSF basis of ASFs with configurations including $3s - 3d$ excitations. The configurations included to the atomic calculations presented here are for Cl^+: [Be]$2p^4(3s^23p^6, 3s^13p^63d^1, 3p^63d^2)$, Cl^{2+}: [Be]$2p^5(3s^03p^6, 3s^13p^5, 3s^23p^4, 3p^53d^1, 3p^43d^2)$ and Cl^{3+}: [Be]$2p^6(3s^03p^4, 3s^13p^3, 3s^23p^2, 3p^33d^1, 3s^13p^23d^1, 3p^23d^2)$.

The *ab initio* *LMM*2 Auger decay spectrum of the isolated Cl atom is shown in Fig. 2(c) as a solid blue line for the 150 to 170 eV energy range. It was obtained by convoluting individual transitions with Lorentzian profiles using their respective Auger decay widths. The complete calculation includes approximately 1.6×10^5 transitions for the *LMM*2 channel. However, only ∼1300 of these contribute with nonzero relative intensity (>0.005%), and 24 have relative intensities of more than 15% of the most intense transition; these dominant transitions are highlighted as filled curves in the same Fig. 2(c) and summarized in Table I. The states *i* and *f* (see Fig. 1) involved in these dominant *LMM*2 transitions are summarized in Table II. For completeness, Table III summarizes the initial *KLL* decay step for i_0 states with the $2p^4$ nonrelativistic electron occupation. 94% of the population of $i_1 - i_9$ states (Table II) is fed through i_{04} $2p^{-2}$ state, which itself receives 92% of the total *KLL* population (Table III). The spectral intensity in the kinetic energy region of 150 to 170 eV accounts for approximately 72% of the total *LMM*2 Auger decay intensity.

2. Cascade population dynamics and long-lived intermediate states

Single core-hole lifetimes in the soft x-ray energy range (such as L-shells of third-row elements, e.g., Cl, S, Ar) are typically shorter than 10 fs [40]. In a single-step Auger process, the population of an intermediate state *i* is created directly by the primary ionization or excitation and is, therefore, proportional to the corresponding ionization or excitation cross section. As a result, the distribution of Auger line intensities is directly proportional to the partial Auger decay rates Γ_{if}. Channels with comparatively small Γ_{if} thus

TABLE I. Theoretical *LMM*2 transitions for Cl atom: Cl^{2+} $[2p^5(3s3p)^6] \rightarrow Cl^{3+}$ $[(3s3p)^4]$. N is the index number of the spectral line, corresponding to the transition from i to f; $\omega_{if}^{(\mathrm{at})}$ is the $i \rightarrow f$ transition energy; $i \rightarrow f$ shows transitions from initial states labeled i_n to final states labeled f_m (see Table II); J_i and J_f are the total angular momentum of i_n and f_m states, respectively; Γ_{if} is the partial Auger decay rate expressed as width in a.u. (1 a.u. = 27.211 eV); I_{if} is the Auger intensity (arb. units), computed as $I_{if} = \frac{\Gamma_{if}}{\sum_f \Gamma_{if}} P_i$, where P_i is the population of state i, $P_i = \sum_{i_0} I_{i_0 i}$ (see Table II); I_{if}^{norm} is the relative intensity (with the maximum normalized to 100); and $\Gamma_i = \sum_f \Gamma_{if}$ is the Auger decay width of the transition (full width at half maximum, FWHM).

N	$\omega_{if}^{(\mathrm{at})}$ (eV)	$i \rightarrow f$	$2J_i$	$2J_f$	Γ_{if} (a.u.)	I_{if} (a.u.)	I_{if}^{norm}	Γ_i (meV)
1	170.58	$i_8 \rightarrow f_5$	5	6	1.34×10^{-03}	0.0253	41	134
2	169.34	$i_6 \rightarrow f_2$	3	4	2.81×10^{-03}	0.0169	27	314
3	168.19	$i_8 \rightarrow f_6$	5	4	5.53×10^{-04}	0.0105	17	134
4	167.82	$i_5 \rightarrow f_2$	5	4	3.01×10^{-03}	0.0380	62	334
5	167.77	$i_4 \rightarrow f_1$	3	2	2.41×10^{-03}	0.0157	25	321
6	167.39	$i_6 \rightarrow f_3$	3	4	2.46×10^{-03}	0.0149	24	314
7	166.94	$i_7 \rightarrow f_5$	5	6	1.69×10^{-03}	0.0114	19	117
8	166.03	$i_9 \rightarrow f_7$	3	4	1.24×10^{-03}	0.0106	17	145
9	165.87	$i_5 \rightarrow f_3$	5	4	4.00×10^{-03}	0.0505	82	334
10	165.71	$i_4 \rightarrow f_3$	3	4	3.65×10^{-03}	0.0237	39	321
11	165.61	$i_2 \rightarrow f_2$	5	4	1.34×10^{-04}	0.0201	33	18
12	164.89	$i_3 \rightarrow f_3$	3	4	4.97×10^{-04}	0.0189	31	43
13	164.37	$i_8 \rightarrow f_7$	5	4	8.13×10^{-04}	0.0154	25	134
14	164.31	$i_6 \rightarrow f_4$	3	0	1.56×10^{-03}	0.0094	15	314
15	163.66	$i_2 \rightarrow f_3$	5	4	2.11×10^{-04}	0.0317	51	18
16	162.38	$i_1 \rightarrow f_3$	7	4	1.04×10^{-04}	0.0616	100	6
17	159.31	$i_1 \rightarrow f_4$	7	0	2.21×10^{-05}	0.0130	21	6
18	156.24	$i_8 \rightarrow f_8$	5	4	6.93×10^{-04}	0.0131	21	134
19	153.06	$i_5 \rightarrow f_5$	5	6	2.03×10^{-03}	0.0257	42	334
20	152.19	$i_6 \rightarrow f_6$	3	4	1.90×10^{-03}	0.0115	19	314
21	150.85	$i_2 \rightarrow f_5$	5	6	1.05×10^{-04}	0.0159	26	18
22	146.86	$i_5 \rightarrow f_7$	5	4	1.31×10^{-03}	0.0165	27	334
23	135.23	$i_1 \rightarrow f_8$	7	4	5.15×10^{-05}	0.0303	49	6
24	120.31	$i_1 \rightarrow f_9$	7	4	2.12×10^{-05}	0.0125	20	6

TABLE II. States involved in the *LMM*2 transitions, summarized in Table I: Populations P_i and P_f; total angular momentum J; nonrelativistic electron occupation; leading electron configuration (jj occupation); lifetime broadening Γ_i (FWHM), given to four decimal places; and lifetime τ_i (fs), computed from the full-precision Γ_i as $\tau_i = 0.658/\Gamma_i$ (eV).

State	Population	J	Electron occupation	Leading electron configuration	Γ_i (eV)	τ_i (fs)
i_1	0.13	7/2	$2p^5 3s^2 3p^4$	$2p^3_{3/2}\,3p^1_{1/2}\,3p^3_{3/2}$	0.0059	112
i_2	0.10	5/2	$2p^5 3s^2 3p^4$	$2p^1_{1/2}\,3p^1_{1/2}\,3p^3_{3/2}$	0.0179	37
i_3	0.06	3/2	$2p^5 3s^2 3p^4$	$2p^3_{3/2}$	0.0431	15
i_4	0.08	3/2	$2p^5 3s^2 3p^4$	$2p^3_{3/2}\,3p^2_{3/2}$	0.3208	2
i_5	0.15	5/2	$2p^5 3s^2 3p^4$	$2p^1_{1/2}\,3p^2_{3/2}$	0.3339	2
i_6	0.07	3/2	$2p^5 3s^2 3p^4$	$2p^1_{1/2}\,3p^1_{1/2}\,3p^3_{3/2}$	0.3141	2
i_7	0.03	5/2	$2p^5 3s^1 3p^5$	$2p^1_{1/2}\,3s^1_{1/2}\,3p^3_{3/2}$	0.1173	6
i_8	0.09	5/2	$2p^5 3s^1 3p^5$	$2p^3_{3/2}\,3s^1_{1/2}\,3p^1_{1/2}$	0.1342	5
i_9	0.05	3/2	$2p^5 3s^1 3p^5$	$2p^1_{1/2}\,3s^1_{1/2}\,3p^3_{3/2}$	0.1453	5
f_1	0.06	1	$3s^2 3p^2$	$3p^1_{1/2}\,3p^1_{3/2}$		
f_2	0.10	2	$3s^2 3p^2$	$3p^2_{3/2}$		
f_3	0.22	2	$3s^2 3p^2$	$3p^1_{1/2}\,3p^1_{3/2}$		
f_4	0.04	0	$3s^2 3p^2$	$3p^2_{3/2}$		
f_5	0.09	3	$3s^1 3p^3$	$3s^1_{1/2}\,3p^1_{1/2}\,3p^2_{3/2}$		
f_6	0.04	2	$3s^1 3p^3$	$3s^1_{1/2}\,3p^3_{3/2}$		
f_7	0.08	2	$3s^1 3p^3$	$3s^1_{1/2}\,3p^1_{1/2}\,3p^2_{3/2}$		
f_8	0.07	2	$3s^0 3p^4$	$3p^1_{1/2}\,3p^3_{3/2}$		
f_9	0.03	2	$3s^0 3p^4$	$3p^2_{3/2}$		

TABLE III. Intermediate states i_0 and theoretical *KLL* transitions $k \to i_0$ for Cl atom: Cl* $[1s^1 2p^6 3s^2 3p^6] \to Cl^{1+}$ $[1s^2 2p^4 3s^2 3p^6]$. Populations $P_{i_0} = \sum_k I_{ki_0}$, *KLL* Auger kinetic energies $\omega_{ki_0}^{(at)}$, partial decay rates Γ_{ki_0}, Auger intensities I_{ki_0}, Auger decay widths $\Gamma_k = \sum_{i_0} \Gamma_{ki_0}$ (FWHM), dominant *LS* terms ($^{2S+1}L_J$), and leading electron configurations (jj occupation). The listed *LS* terms are dominant components and do not represent fully coupled configuration state functions.

State	Population	$\omega_{ki_0}^{(at)}$ (eV)	Γ_{ki_0} (a.u.)	I_{ki_0} (arb. units)	Γ_k (meV)	*LS* term	Leading electron configuration[a]
i_{01}	0.01	2391.4	8.90×10^{-5}	8.52×10^{-3}	284	$^3P_2$	$2p_{1/2}^2 2p_{3/2}^2$
i_{02}	0.00	2390.1	7.52×10^{-7}	7.20×10^{-5}	284	$^3P_1$	$2p_{1/2}^1 2p_{3/2}^3$
i_{03}	0.00	2389.7	5.49×10^{-6}	5.26×10^{-4}	284	$^3P_0$	$2p_{1/2}^0 2p_{3/2}^4$
i_{04}	0.92	2383.4	9.58×10^{-3}	9.17×10^{-1}	284	$^1D_2$	$2p_{1/2}^1 2p_{3/2}^3$
i_{05}	0.07	2372.3	7.50×10^{-4}	7.18×10^{-2}	284	$^1S_0$	$2p_{1/2}^2 2p_{3/2}^2$

[a]Note that only the $^3P_1$ term corresponds to a pure $2p_{1/2}^1 2p_{3/2}^3$ configuration; all other terms are strongly mixed (see Appendix B). This reflects the weak spin-orbit interaction compared with electrostatic angular-momentum coupling in low-Z atoms (∼1−2 eV vs ∼8−10 eV in Ar, respectively [39]).

contribute negligibly to the spectrum, as observed for the first *KLL* Auger decay step (see Table III).

In a cascade, however, the intermediate state i is populated through sequential transitions, $k \to i_0$ followed by $i_0 \to i$ (see Fig. 1). The intensity I_{if} of the $i \to f$ Auger line is then determined by

$$I_{if} = \frac{\Gamma_{if}}{\Gamma_i} P_i,$$

where P_i is the population of the state i generated by preceding cascade steps and Γ_i is its total decay width, obtained by summing over all energetically allowed radiative and radiationless transitions. Thus, a decay channel with a comparatively small partial width Γ_{if} (see Table I) can dominate the observable Auger spectrum in a cascade. This situation arises when (i) the preceding decay steps efficiently funnel population into the intermediate level i (large P_i), such that i accumulates population from earlier cascade stages that provide few rapid decay pathways (see Table II), and (ii) the set of energetically accessible final states f from i is limited or characterized by small partial Auger decay rates (reduced orbital overlap, angular-momentum constraints, configuration interaction effects, or related selection rules).

Consequently, lifetimes on the order of $\sim 10^2$ fs for cascade intermediates containing a $2p^{-1}$ vacancy, although seemingly anomalous when compared to single-step decays, are fully consistent with the underlying cascade population dynamics and with the calculated distribution of partial decay rates [28–30,41,42].

B. Influence of dissociation dynamics on Auger spectra

Ultrafast dissociation effects in resonant x-ray scattering have so far been investigated primarily in systems where all relevant electronic states exhibit short-range dissociative PECs [18–24,26,27,33]. In such systems, spectral profiles typically consist of a broad molecular band originating from decay near the equilibrium bond length R_0, together with narrow atomic lines formed once the fragments have separated sufficiently to behave as effectively isolated species [19–24,26]. However, this picture no longer applies to systems with long-range interactions, such as the Coulomb repulsion between charged fragments in the HCl molecule studied here. In this case, the PECs remain repulsive even at large internuclear distances, preventing the fragments from reaching a truly noninteracting asymptotic limit. As a result, the mechanisms of spectral formation in RAC and NAC differ qualitatively.

To rationalize the pronounced spectral differences between Figs. 2(a) and 2(d), despite both processes occurring in the ultrafast dissociation regime, and to elucidate the fundamentally different fragment interactions governing the final *LMM*2 Auger decay step, we first outline a qualitative theoretical framework below. This description is then refined through advanced calculations of the *LMM*2 Auger spectrum of an isolated Cl atom, combined with semiclassical wave-packet propagation on both *ab initio* and model Coulomb PECs for HCl (see Sec. IV C).

1. *Short-range fragment interactions in resonant Auger cascades*

In RAC, the final *LMM*2 Auger transition $i \to f$ occurs at an internuclear distance R between dissociating molecular states asymptotically corresponding to $H^0 - Cl^{2+}$ and $H^0 - Cl^{3+}$, respectively. Because the interaction between neutral hydrogen and Cl^{n+} $(n = 2, 3)$ is short range, the transition energy $\omega_{if}(R) = E_i(R) - E_f(R)$ rapidly converges to its atomic limit $\omega_{if}^{(at)} = \omega_{if}(\infty)$,

$$\omega_{if}(R) \to \omega_{if}^{(at)}; \quad R - R_0 \sim 1 \text{ a.u.}; \quad \Delta\omega \approx \Gamma_i. \qquad (1)$$

Here, the spectral broadening $\Delta\omega$ is set by the decay rate Γ_i (inverse lifetime $\Gamma_i = 1/\tau_i$) of the intermediate state i [20,21,43]. As a consequence, convergence to the atomic limit is reached already a few atomic units beyond R_0, and the position of the atomic-like peak becomes largely insensitive to Γ_i (Fig. 3).

Consistent with this picture, the calculated *LMM*2 Auger spectrum of isolated atomic Cl reproduces the main atomic-like features observed in the HCl RAC spectrum, although small relative energy shifts remain [Figs. 2(c) and 2(d)]. This demonstrates that the positions of the atomic lines associated with the Cl fragment are largely unaffected by the nuclear dynamics during dissociation.

2. *Long-range fragment interactions in non-resonant Auger cascades*

In contrast, following Cl 1*s* ionization in the NAC process, the HCl molecule dissociates into ion pairs: $H^+ + Cl^{2+}$ in the intermediate state $(Z_i = 2)$ and $H^+ + Cl^{3+}$ in the final

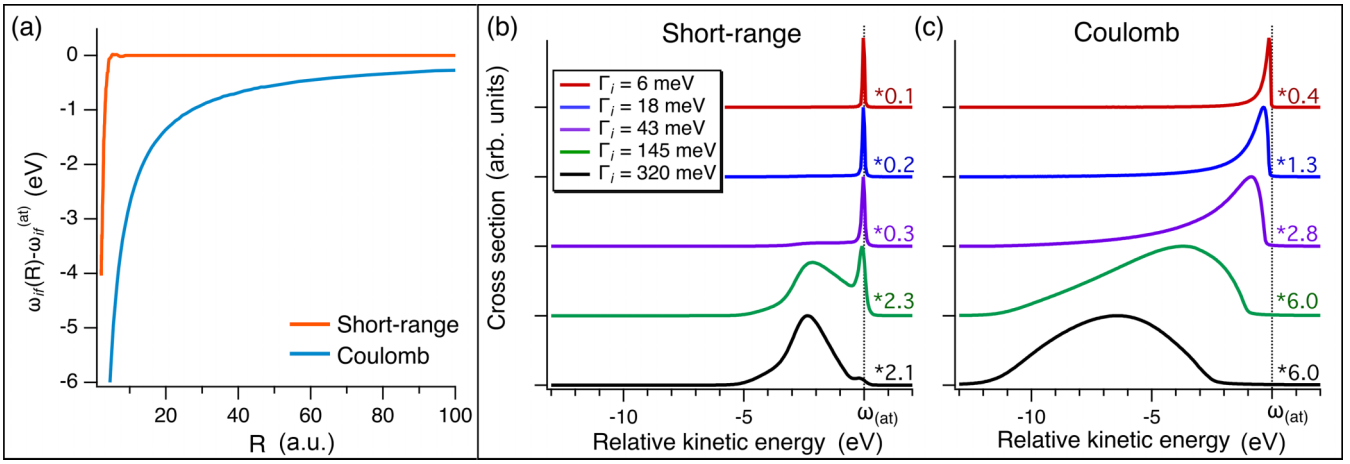

FIG. 3. (a) Energy shift $\omega_{if}(R) - \omega_{if}^{(at)}$ as a function of internuclear distance R for short-range (orange) and long-range Coulomb (blue) potentials, where $\omega_{if}^{(at)}$ is the atomic-limit transition energy between intermediate i and final f states. (b), (c) Simulated Auger cross sections $\sigma_{if}(E)$, or spectral profiles, for (b) short-range and (c) long-range Coulomb potentials as a function of Γ_i. Cross sections are modeled using (b) the quantum wave-packet technique [20,21], employing short-range dissociative PECs for the $2p^{-1}\sigma^*$ core-excited and $^4\Pi$ final state of HCl; and (c) Eq. (5), employing long-range Coulomb PECs. All spectra in (b), (c) are normalized to unit area and further scaled so that maxima equal to 1, with scaling factors indicated.

state ($Z_f = 3$). Unlike in short-range potentials characterised by Eq. (1) long-range Coulomb repulsion between charged fragments persists throughout the dissociation, making the transition energy $\omega_{if}(R)$ strongly distance dependent. As a result, it converges to its atomic limit $\omega_{if}^{(at)}$ only at very large separations ($R \gg R_0$), where the difference between the relevant Coulomb interactions becomes negligible [Fig. 3(a)]:

$$\omega_{if}(R) \to \omega_{if}^{(at)} - \frac{1}{R};\ R - R_0 \sim 100\ \text{a.u.};\ \Delta\omega \sim \frac{1}{R}. \quad (2)$$

As shown in Fig. 3(a), this Coulomb-induced energy shift remains significant up to internuclear separations of $R \gtrsim 100$ a.u.

Only beyond a critical distance $R_{at} \sim 200$ to 300 a.u., which is accessible only to sufficiently long-lived (metastable) intermediate states, does the Coulomb interaction drop below ~0.1 eV, allowing sharp atomic-like spectral features to emerge. However, the long-range Coulomb interaction is expected to lead to asymmetry and broadening of the atomic-like lines arising from possible metastable states.

3. Lifetime-dependent Auger line shapes under long-range Coulomb interactions

Since the propagation distance of the dissociating fragments can be estimated as $R \sim v_{i\infty}\tau_i = v_{i\infty}/\Gamma_i$ (see the general solution in Appendix A), where $v_{i\infty} = \sqrt{2Z_i/\mu R_0}$ is the asymptotic relative velocity of the fragments for an intermediate charge Z_i and reduced mass μ, the Coulomb-induced spectral shift $1/R$ and the associated broadening $\Delta\omega$ can be estimated as

$$\frac{1}{R} \sim \Delta\omega \sim \frac{\Gamma_i}{v_{i\infty}}. \quad (3)$$

The gradual decrease of the Coulomb shift $1/R$ from its initial value $1/R_0$ towards zero during dissociation results in an asymmetric spectral profile with a characteristic low-energy tail. This behavior provides a qualitative explanation for the observed evolution of the Auger line shape as the lifetime of the intermediate state Γ_i varies [Fig. 3(c)].

In contrast to short-range potentials Eq. (1), long-range Coulomb interactions Eq. (2) make both the peak position and the linewidth strongly sensitive to nuclear dynamics, through the fragmentation velocity and the intermediate-state lifetime. Within this simple theoretical framework, the coupling between electronic decay and nuclear motion naturally produces red-shifted and broadened Auger lines, thereby suppressing the formation of well-resolved fragment peaks characteristic of systems without long-range interactions.

C. Modeling of NAC line profiles

To simulate the role of nuclear dynamics in shaping the NAC spectrum we develop a semiclassical expression for the Auger decay cascade cross section that follows nuclear trajectories on successive potential-energy curves and includes the Coulomb interaction between dissociating fragments. The semiclassical approach is a deliberate and well-motivated choice. First, a full quantum wave-packet treatment of the complete Auger cascade would require tracking a huge number of intermediate states, making such calculations computationally very expensive. Second, we benchmarked the semiclassical approach against full wave-packet calculations for representative single dissociative final states and obtained very good agreement. Third, the semiclassical framework provides direct physical insight into how cascade population dynamics, decay rates, and evolving Coulomb potentials shape Auger spectra, insight that would be difficult to extract from purely numerical wave-packet simulations. The approach is, therefore, not a limitation, but an effective and physically transparent tool for addressing the problem at hand. We apply this approach to the 24 dominant *LMM*2 transitions listed in Table I, using both *ab initio* PECs and model Coulomb PECs.

1. Semiclassical description of cascade dynamics

The process begins with excitation to a short-lived bound core-excited state, which decays via ultrafast *KLL* Auger transition ($\tau \sim 1$ fs) to a dissociative intermediate state i_0 (see Fig. 1). Due to $1s^{-1}$ short lifetime [44], this step can be treated as an instantaneous transition from the ground state to i_0, with the probability $P(R_0' - R_0) = \exp[-(R_0' - R_0)^2/a^2]$ of transition from the ground-state equilibrium R_0 to a point R_0' on the PEC i_0, where a is the width of the ground-state vibrational wave function. From R_0', the wave packet propagates along the PEC of the i_0 state to a point R' with the probability $W_{i_0}(R_0', R')$, where the *LMM*1 Auger decay projects it onto the PEC of state i. It then evolves along the PEC of i to an internuclear distance R with the probability $W_i(R', R)$, where the final *LMM*2 Auger decay occurs, populating the final state f (see Fig. 1). The probability of the full cascade process is given by the product of two propagation probabilities and a Lorentzian describing the *LMM*2 Auger decay on the last step of the cascade

$$W_{i_0}(R_0', R') \times W_i(R', R) \Big/ \left\{[E - \omega_{if}(R)]^2 + \Gamma_i^2/4\right\}.$$

The total Auger cross section can then be expressed as

$$\sigma(E) = \sum_{if} I_{if}\sigma_{if}(E); \quad \text{with } I_{if} = \frac{\Gamma_{if}}{\Gamma_i} P_i, \tag{4}$$

where I_{if} is the intensity of the $i \to f$ transition, Γ_{if} is the partial Auger decay rate, P_i is the population of the state i, and Γ_i is the Ager decay width (see Table I). The spectral profile of each $i \to f$ transition is defined by the partial cross section $\sigma_{if}(E)$

$$\sigma_{if}(E) = \int_0^\infty dR_0' P(R_0' - R_0) \int_{R_0'}^\infty dR' W_{i_0}(R_0', R') \times \int_{R'}^\infty dR \, \frac{W_i(R', R)}{[E - \omega_{if}(R)]^2 + \frac{\Gamma_i^2}{4}}. \tag{5}$$

The propagation probability $W_i(R', R)$ exponentially depends on the ratio of the propagation time $t_i(R', R)$ and the lifetime of the corresponding state τ_i:

$$W_i(R', R) = e^{-\Gamma_i t_i(R', R)}; \; t_i(R', R) = \int_{R'}^{R} \frac{dR''}{v_i(R', R'')}. \tag{6}$$

Here and below we neglect small lifetime broadening of the final state f; μ is the reduced mass and $v_i(R', R'') = \sqrt{(2/\mu)[E_i(R') - E_i(R'')]}$ is the relative velocity at the internuclear distance R''.

Figure 4 shows the propagation probability $W_i(R', R)$ for various intermediate state widths Γ_i. Only the metastable intermediate state with $\Gamma_i = 6$ meV ($\tau_i = 112$ fs) reaches large internuclear distances ($R_{\text{at}} \sim 300$ a.u.), where the difference in the Coulomb interactions becomes negligible, allowing narrow atomic peaks to form. Shorter-lived states decay earlier, preventing the system from reaching the atomic limit (where the Coulomb shift $1/\text{R} \lesssim 0.1$ eV). Consequently, their Auger profiles are broadened and shifted toward lower energies.

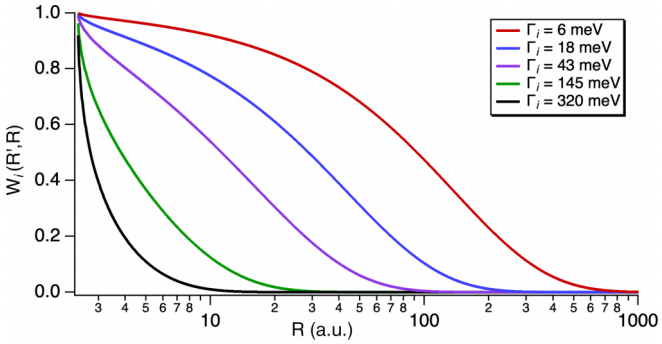

FIG. 4. Dependence of propagation probability $W_i(R', R)$ from R' to R along $E_i(R)$, on the lifetime $\tau_i = 1/\Gamma_i$. Calculations are performed using Eqs. (6) and (A1). Here we use $R' = R_0$.

2. Modeling of ab initio potential energy curves

The *ab initio* PECs were computed at the Complete Active Space Self-Consistent Field (CASSCF) level as implemented in MOLPRO [45] with an aug-cc-pcvdz basis set [46,47]. Relativistic corrections were included using the Douglas-Kroll Hamiltonian [48–50]. Except for the 1*s* and 2*s* electrons of Cl, all electrons were included in the active space. The number of orbitals employed in the active space was chosen 9 and 13 when computing $2p^{-2}$ and $2p^{-1}V^{-2}$ states, respectively. The calculated PECs for the intermediate i_0 states of HCl^{2+} [Cl $2p^{-2}$] and the i states of HCl^{3+} [$2p^{-1}V^{-2}$] have a strong covalent character around the equilibrium bond length R_0. At larger internuclear distances, the PECs of the i_0, i, and final f states follow Coulombic forms: $\omega_{i_0}^{(\text{at})} + \frac{1}{R}$, $\omega_i^{(\text{at})} + \frac{2}{R}$, and $\omega_f^{(\text{at})} + \frac{3}{R}$, respectively.

Figure 5(a) displays the PECs, referenced to their respective asymptotic atomic limits at $R \to \infty$. The *ab initio* PECs for the i_0 and i states are shown as solid lines, while the model Coulomb potentials (Z/R) are shown as dotted lines.

3. Comparison of the simulated NAC decay spectra using ab initio and pure Coulomb potentials

Because of the complexity of the multielectronic configurations involved, a direct assignment of the computed PECs to specific intermediate states with well-defined atomic asymptotes (Table I) is not feasible. To assess the influence of the PEC shape on NAC line profiles, we, therefore, selected a set of *ab initio* PECs that exhibit the largest deviations from pure Coulomb potentials at small internuclear distances, where covalent interactions are most pronounced [see Fig. 5(a)]. These PECs represent limiting cases of short-range behavior, while the pure Coulomb potentials capture the asymptotic long-range interaction. The actual physical situation is expected to lie between these two extremes. A comparison of NAC spectra simulated using *ab initio* and pure Coulomb PECs allows short-range bonding effects to be disentangled from long-range Coulomb interactions. The covalent region near the equilibrium distance R_0 plays a significant role only when decay occurs at small internuclear separations, i.e., for intermediate states i with short

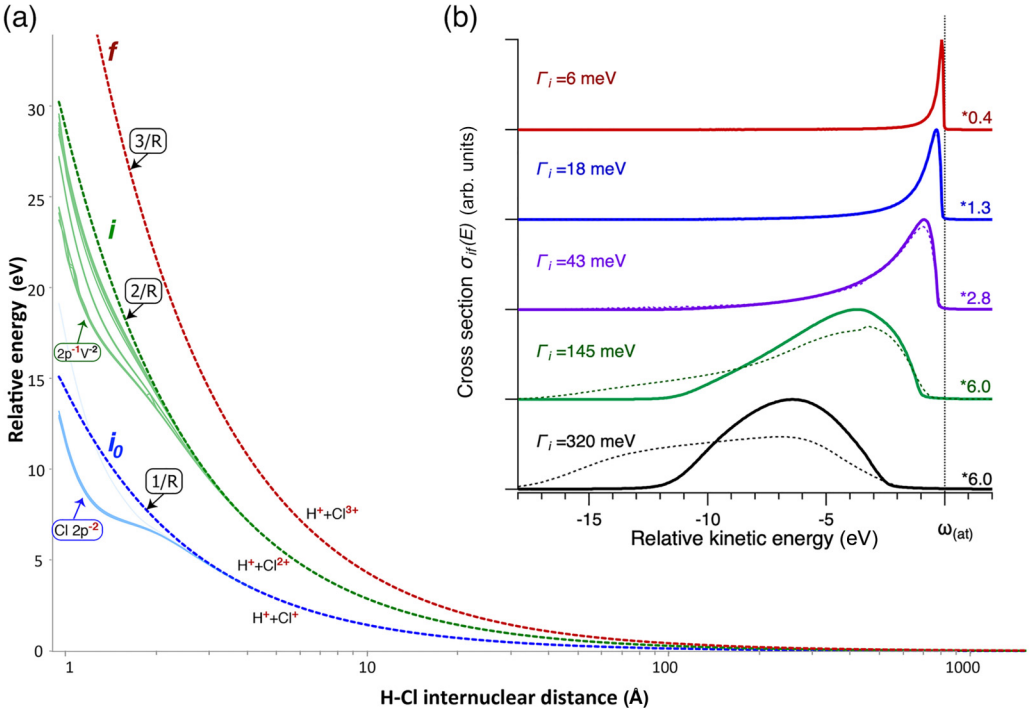

FIG. 5. (a) PECs for the intermediate i_0 (HCl^{2+}, Cl $2p^{-2}$), i (HCl^{3+}, $2p^{-1}V^{-2}$), and final f (HCl^{4+}, V^{-4}) states, plotted relative to their asymptotic atomic energies at $R \to \infty$. The final f states are modeled by a pure Coulomb potential $3/R$ only. Solid lines represent *ab initio* PECs, and dotted lines denote the corresponding Coulomb potentials Z/R. Strong deviations from the Coulomb form at short internuclear distances ($R \sim R_0$) reflect covalent interactions, which notably affect the Auger line shapes for large Γ_i. (b) Calculated NAC line profiles for selected Γ_i values using *ab initio* (dotted lines) and pure Coulomb (solid lines) PECs. The influence of short-range covalent interactions, present in the *ab initio* PECs, is significant only for large Γ_i of 320 meV, while for intermediate and small lifetime broadening ($\Gamma_i < 100$ meV), the line shapes are nearly identical. The underlying dynamics were modeled using semiclassical wave-packet propagation on the respective PECs using Eq. (5).

lifetimes $\tau_i = 1/\Gamma_i$, before well-separated atomic fragments are formed.

Auger line profiles calculated for different values of Γ_i using Eq. (5) are shown in Fig. 5(b). Solid curves correspond to simulations using pure Coulomb potentials [also shown in Fig. 3(c)], while dotted curves are obtained with *ab initio* PECs. Deviations at small R significantly affect only states with large Γ_i, whereas the line shapes for intermediate and small Γ_i are nearly indistinguishable for the two types of potentials.

The total simulated NAC spectra obtained with *ab initio* and pure Coulomb PECs are compared in Figs. 6(a) and 6(b), respectively. The most pronounced difference appears in the broad background component (gray filled curves), which is dominated by contributions from states with the largest Γ_i. It should be noted that semiclassical wave-packet propagation tends to overestimate contributions from near-equilibrium distances ($R \sim R_0$), where the fragment velocity is low and the system spends a disproportionately long time [24].

Overall, simulations based on pure Coulomb potentials show better agreement with the experimental spectra. This can be attributed to (i) the limited representativeness of the selected *ab initio* PECs for the full set of intermediate NAC states, and (ii) an inherent tendency of the semiclassical approach to overemphasize decay contributions from the small-R region near R_0.

V. DISCUSSION: SPECTRAL SIGNATURES OF INTERMEDIATE-STATE DYNAMICS IN NAC

A comparison of the theoretical NAC spectrum [Fig. 2(b)] with the atomic Cl^{2+} spectrum [Fig. 2(c)] highlights the distinct spectral signatures of transitions from long- and short-lived intermediate states. As expected, the positions of long-lived atomic transitions of Cl^{2+} [$A_{1,2}$, Fig. 2(c)] remain essentially unaffected by nuclear motion during the Coulomb explosion of HCl^{3+} [$A_{1,2}$, Fig. 2(b)]. In contrast, short-lived states ($\Gamma_i = 314$–334 meV) decay at internuclear distances $R < 10$ a.u., causing pronounced dynamical broadening of about 8 eV. This broadening produces the gray-shaded background in Fig. 2(b) and is accompanied by a substantial red shift of comparable magnitude relative to the corresponding atomic transitions in the RAC spectrum, marked as gray-shaded peaks $B_{1,2,3}$ in Fig. 2(c). States with intermediate lifetimes ($\Gamma_i = 18$ meV), shown as filled blue curves, exhibit only slight red shifts and moderate broadening, and are likely responsible for the shoulders observed in the experimental NAC spectrum [Fig. 2(a)].

Our *LMM*2 Auger calculations (Table I) show that most *LMM*2 channels are short-lived ($\tau_i \sim 2$ to 6 fs, $\Gamma_i \sim 120$ to 330 meV), thus contributing to the broad, red-shifted background observed in NAC in contrast to RAC spectrum (see Fig. 2). Notably, within the studied energy range (150 to 170 eV), only two transitions exhibit narrow widths

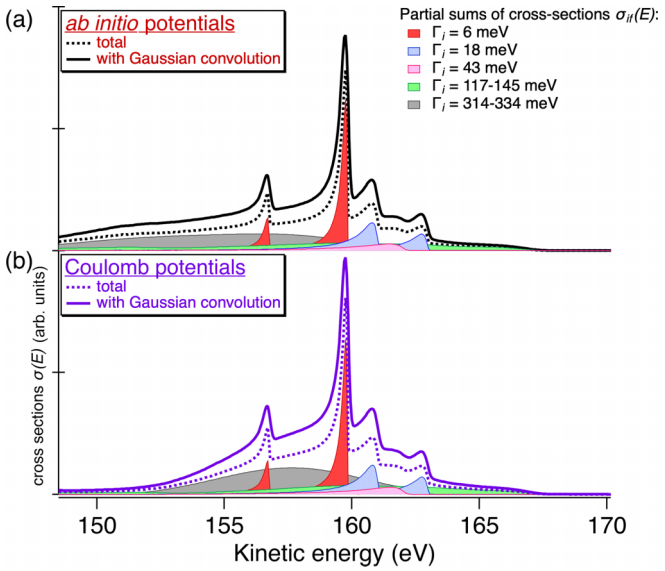

FIG. 6. Simulated NAC spectra using long-range (a) *ab initio* PECs and (b) pure Coulomb PECs. Dotted line corresponds the total NAC spectrum; solid lines show the same spectrum convolved with a 0.2-eV FWHM Gaussian to approximate experimental resolution. Filled curves represent transitions with relative intensities $\geqslant$15% (Table I), grouped by Auger decay widths and summed accordingly: $\Gamma_i = 6$ (red), 18 (blue), 43 (pink), 117 to 145 (green), and 314 to 334 (gray) meV. All spectra are shifted by −2.5 eV.

($\Gamma_i = 6\,\text{meV}$, $\tau_i = 112$ fs), both originating from the same $[2p^5 3s^2 3p^4]$ i state with total angular momentum $J_i = 7/2$, which accumulates a dominant population P_i in the cascade (Table II). This state is isoelectronic to Ar^{3+} $[2p^5 3s^2 3p^4]$, which exhibits a comparable decay width ($\Gamma_i \approx 6.5$ meV) and similarly dominates the atomic *LMM*2 spectrum [31]. The long lifetime of this state in Cl^{2+} enables the observation of sharp atomic lines (A_1 and A_2, Fig. 2) within the molecular Auger cascade spectrum of HCl.

These results align with our recent fluorescence studies of SF_6, where S K-shell ionization leads to complete dissociation during the cascade that proceeds via intermediate states with a S $2p$ core-electron vacancy [11]. Similar to HCl, the formation of atomic sulfur in SF_6 suggests that metastable core-hole intermediates arise during the electronic decay cascade, allowing sufficient time for dissociation prior to the final decay step. Since in radiative transitions, i.e., photon emission, the final $i \to f$ step preserves the charge state, inelastic x-ray scattering may provide enhanced sensitivity to nuclear motion during cascades.

VI. CONCLUSION

In conclusion, we show experimentally and theoretically that nuclear dynamics during Auger cascades play a decisive role in shaping the spectra. In particular, we identify a qualitative distinction between fragmentation driven by short-range repulsive potentials, as in resonant Auger decay, and long-range Coulomb explosion following deep-core ionization. In the latter case, extended Coulomb interactions prevent the system from reaching the dissociative limit within the lifetime of most intermediate states, producing broad, red-shifted features rather than sharp atomic lines, except for a few metastable states that survive to internuclear distances exceeding 100 a.u.

Our study of HCl demonstrates that the appearance of atomic lines from long-lived intermediate states provides direct insight into the interplay of nuclear dynamics and long-range Coulomb forces, thereby filling a missing element in the dynamical picture of molecular Coulomb fragmentation. This description can guide future time-resolved pump-probe experiments in mapping the fragmentation dynamics and Coulomb interactions, tracing the spatial and temporal evolution of intermediate states through the Auger line profiles.

ACKNOWLEDGMENTS

Experiments were performed at the GALAXIES beamline at SOLEIL Synchrotron, France (Proposals No. 20120122 and No. 99150133). We are grateful to SOLEIL staff for smoothly running the facility. O.T. and V.K. acknowledge the Swedish Foundation for International Cooperation in Research and Higher Education (STINT) (Project No. MG2021-9085). F.G. acknowledges the Russian Science Foundation (Project No. 25-12-00148). J.L. thanks National Natural Science Foundation of China, No. 12541505 and No. 12211530044. The computations were enabled by resources provided by the National Academic Infrastructure for Supercomputing in Sweden (NAISS), partially funded by the Swedish Research Council through Grant No. 2022-06725.

DATA AVAILABILITY

The data that support the findings of this article are not publicly available upon publication because it is not technically feasible and/or the cost of preparing, depositing, and hosting the data would be prohibitive within the terms of this research project. The data are available from the authors upon reasonable request.

APPENDIX A: CLASSICAL TRAVELING TIME AND PROPAGATION DISTANCE FOR THE COULOMB MODEL

For a purely Coulomb repulsive potential, the dissociating fragments initially possess potential energy $U_0 = Z_i/R_0$, where Z_i is the charge of the intermediate ionic fragment and R_0 is the initial internuclear (interfragment) distance. As the fragments separate, this potential energy is converted into relative kinetic energy. Assuming a reduced mass μ, energy conservation yields $\mu v_{i\infty}^2/2 = Z_i/R_0$, which defines the asymptotic relative velocity

$$v_{i\infty} = \sqrt{\frac{2Z_i}{\mu R_0}},$$

reached at infinite separation ($R \to \infty$, $U_\infty \to 0$). The classical propagation time from R_0 to a distance R can be obtained

as

$$t_i(R_0, R) = \sqrt{\frac{\mu}{2Z_i}} \int_{R_0}^{R} \frac{dR'}{\sqrt{\frac{1}{R_0} - \frac{1}{R}}}$$
$$= \frac{R_0}{v_{i\infty}} [\sqrt{\rho(\rho+1)} + \ln(\sqrt{\rho} + \ln(\sqrt{\rho} + \sqrt{\rho+1})],$$
$$\rho = \frac{R - R_0}{R_0}. \quad \text{(A1)}$$

Since the lifetime $\tau_i = 1/\Gamma_i$ sets the characteristic time window for Auger decay, the propagation time may be approximated by $t_i(R_0, R) \approx \tau_i = 1/\Gamma_i$. This yields an implicit equation for the distance R reached during the lifetime of the ith intermediate state

$$\sqrt{\rho(\rho+1)} + \ln(\sqrt{\rho} + \ln(\sqrt{\rho} + \sqrt{\rho+1}) = \frac{v_{i\infty}}{\Gamma_i R_0}. \quad \text{(A2)}$$

In general, Eq. (A2) must be solved numerically. However, two physically relevant limiting cases admit simple analytical expressions using Eq. (A1)

$$R - R_0 \approx \frac{v_{i\infty}}{\Gamma_i} \quad \text{for} \quad \frac{v_{i\infty}}{\Gamma_i} \gg R_0, \quad \text{and}$$
$$R - R_0 \approx R_0 \left(\frac{v_{i\infty}}{\Gamma_i R_0}\right)^2 \quad \text{for} \quad \frac{v_{i\infty}}{\Gamma_i} \ll R_0. \quad \text{(A3)}$$

Because Auger decay from the ith state follows an exponential time distribution with time constant τ_i, the measured spectrum samples internuclear distances reached during dissociation on the corresponding repulsive potential. For short-lived states (large Γ_i), decay occurs predominantly at small R, producing an asymmetric low-energy tail that grows with increasing Γ_i. This behavior provides a qualitative explanation for the observed evolution of the spectral line shapes as a function of the intermediate-state lifetime [see Fig. 3(c)].

While this classical Coulomb model offers an intuitive understanding of the red-shifted and broadened Auger lines observed experimentally, the *ab initio* calculations presented in the main text provide a more accurate description of the full dynamical effects and Auger line profiles in the presence of long-range Coulomb interactions.

APPENDIX B: ELECTRON CONFIGURATIONS FOR i_0 TERMS IN JJ-COUPLING SCHEME

Full electronic configurations for the *LS* terms assigned in Table III

$$^3P_2 = \sqrt{\frac{2}{3}}\, 2p^2_{1/2} 2p^2_{3/2} - \sqrt{\frac{1}{3}}\, 2p^1_{1/2} 2p^3_{3/2};$$
$$^3P_1 = 2p^1_{1/2} 2p^3_{3/2};$$
$$^3P_0 = -\sqrt{\frac{1}{3}}\, 2p^2_{1/2} 2p^2_{3/2} + \sqrt{\frac{2}{3}}\, 2p^0_{1/2} 2p^4_{3/2};$$
$$^1D_2 = \sqrt{\frac{1}{3}}\, 2p^2_{1/2} 2p^2_{3/2} + \sqrt{\frac{2}{3}}\, 2p^1_{1/2} 2p^3_{3/2};$$
$$^1S_0 = \sqrt{\frac{2}{3}}\, 2p^2_{1/2} 2p^2_{3/2} + \sqrt{\frac{1}{3}}\, 2p^0_{1/2} 2p^4_{3/2}.$$

[1] T. A. Carlson, in *Desorption Induced by Electronic Transitions DIET I*, edited by N. H. Tolk, M. M. Traum, J. C. Tully, and T. E. Madey (Springer, Berlin, 1983), pp. 169–182.

[2] J. W. McManus, F. Allum, J. Featherstone, C. Lam, and M. Brouard, J. Phys. Chem. A **128**, 3220 (2024).

[3] H. Yuan, Y. Gao, B. Yang, S. Gu, H. Lin, D. Guo, J. Liu, S. Zhang, X. Ma, *et al.*, Phys. Rev. Lett. **133**, 193002 (2024).

[4] C. A. Schouder, A. S. Chatterley, J. D. Pickering, and H. Stapelfeldt, Annu. Rev. Phys. Chem. **73**, 323 (2022).

[5] S. Kazandjian, J. Rist, M. Weller, F. Wiegandt, D. Aslitürk, S. Grundmann, M. Kircher, G. Nalin, D. Pitters, I. Vela Pérez, M. Waitz, G. Schiwietz, B. Griffin, J. B. Williams, R. Dörner, M. Schöffler, T. Miteva, F. Trinter, T. Jahnke, and N. Sisourat, Phys. Rev. A **98**, 050701(R) (2018).

[6] B. Liu and Y. Yang, Appl. Sci. **12**, 5014 (2022).

[7] M. N. Piancastelli, T. Marchenko, R. Guillemin, L. Journel, O. Travnikova, I. Ismail, and M. Simon, Rep. Prog. Phys. **83**, 016401 (2020).

[8] N. Boudjemia, K. Jänkälä, T. Gejo, K. Nagaya, K. Tamasaku, M. Huttula, M. N. Piancastelli, M. Simon, and M. Oura, Phys. Chem. Chem. Phys. **21**, 5448 (2019).

[9] S. Kosugi, F. Koike, M. Iizawa, M. Oura, T. Gejo, K. Tamasaku, J. R. Harries, R. Guillemin, M. N. Piancastelli, M. Simon, and Y. Azuma, Phys. Rev. Lett. **124**, 183001 (2020).

[10] P. J. Ho, D. Ray, C. S. Lehmann, A. E. A. Fouda, R. W. Dunford, E. P. Kanter, G. Doumy, L. Young, D. A. Walko, X. Zheng, L. Cheng, and S. H. Southworth, J. Chem. Phys. **158**, 134304 (2023).

[11] O. Travnikova, F. Trinter, M. Agåker, G. Visentin, J. Andersson, L. Kjellsson, I. Ismail, N. Velasquez, D. Koulentianos, M. Harder, Z. Yin, J. Söderström, T. Marchenko, R. Guillemin, O. D. McGinnis, H. Ågren, S. Fritzsche, M. Simon, J.-E. Rubensson, and J. Nordgren, Phys. Rev. Lett. **134**, 063003 (2025).

[12] S. Carniato, R. Püttner, I. Ismail, D. Peng, O. Travnikova, T. Marchenko, R. Guillemin, D. Céolin, A. Verma, N. Velasquez, M. Meyer, M. N. Piancastelli, and M. Simon, J. Phys. Chem. Lett. **16**, 9362 (2025).

[13] B. Richard, R. Boll, S. Banerjee, J. M. Schäfer, Z. Jurek, G. Kastirke, K. Fehre, M. S. Schöffler, N. Anders, T. M. Baumann, S. Eckart, B. Erk, A. D. Fanis, R. Dörner, S. Grundmann, P. Grychtol, M. Hofmann, M. Ilchen, M. Kircher, K. Kubicek, *et al.*, Science **389**, 650 (2025).

[14] L. Fang, T. Osipov, B. Murphy, F. Tarantelli, E. Kukk, J. P. Cryan, M. Glownia, P. H. Bucksbaum, R. N. Coffee, M. Chen, C. Buth, and N. Berrah, Phys. Rev. Lett. **109**, 263001 (2012).

[15] B. Rudek, S.-K. Son, L. Foucar, S. W. Epp, B. Erk, R. Hartmann, M. Adolph, R. Andritschke, A. Aquila, N. Berrah, C. Bostedt, J. Bozek, N. Coppola, F. Filsinger, H. Gorke, T. Gorkhover, H. Graafsma, L. Gumprecht, A. Hartmann, G. Hauser, *et al.*, Nat. Photon. **6**, 858 (2012).

[16] A. Rudenko, L. Inhester, K. Hanasaki, X. Li, S. J. Robatjazi, B. Erk, R. Boll, K. Toyota, Y. Hao, O. Vendrell, C. Bomme,

E. Savelyev, B. Rudek, L. Foucar, S. H. Southworth, C. S. Lehmann, B. Kraessig, T. Marchenko, M. Simon, K. Ueda, *et al.*, Nature (London) **546**, 129 (2017).
[17] T. J. A. Wolf, F. Holzmeier, I. Wagner, N. Berrah, C. Bostedt, J. Bozek, P. Bucksbaum, R. Coffee, J. Cryan, J. Farrell, R. Feifel, T. J. Martinez, B. McFarland, M. Mucke, S. Nandi, F. Tarantelli, I. Fischer, and M. Gühr, Appl. Sci. **7**, 681 (2017).
[18] J. Stöhr, *The Nature of X-Rays and Their Interactions with Matter*, 1st ed. (Springer, New York, 2023).
[19] P. Morin and I. Nenner, Phys. Rev. Lett. **56**, 1913 (1986).
[20] P. Sałek, F. Gel'mekhanov, and H. Ågren, Phys. Rev. A **59**, 1147 (1999).
[21] F. Gel'mukhanov, M. Odelius, S. P. Polyutov, A. Föhlisch, and V. Kimberg, Rev. Mod. Phys. **93**, 035001 (2021).
[22] E. Kukk, H. Aksela, O.-P. Sairanen, S. Aksela, A. Kivimäki, E. Nõmmiste, A. Ausmees, A. Kikas, S. J. Osborne, and S. Svensson, J. Chem. Phys. **104**, 4475 (1996).
[23] H. Sann, T. Havermeier, C. Müller, H.-K. Kim, F. Trinter, M. Waitz, J. Voigtsberger, F. Sturm, T. Bauer, R. Wallauer, D. Schneider, M. Weller, C. Goihl, J. Tross, K. Cole, J. Wu, M. S. Schöffler, H. Schmidt-Böcking, T. Jahnke, M. Simon, *et al.*, Phys. Rev. Lett. **117**, 243002 (2016).
[24] M. Hrast, M. Ljubotina, and M. Žitnik, Phys. Chem. Chem. Phys. **27**, 1473 (2025).
[25] E. Ertan, V. Savchenko, N. Ignatova, V. Vaz da Cruz, R. C. Couto, S. Eckert, M. Fondell, M. Dantz, B. Kennedy, T. Schmitt, A. Pietzsch, A. Föhlisch, F. Gel'mukhanov, M. Odelius, and V. Kimberg, Phys. Chem. Chem. Phys. **20**, 14384 (2018).
[26] O. Travnikova, V. Kimberg, R. Flammini, X.-J. Liu, M. Patanen, C. Nicolas, S. Svensson, and C. Miron, J. Phys. Chem. Lett. **4**, 2361 (2013).
[27] O. Travnikova, E. Kukk, F. Hosseini, S. Granroth, E. Itälä, T. Marchenko, R. Guillemin, I. Ismail, R. Moussaoui, L. Journel, J. Bozek, R. Püttner, P. Krasnov, V. Kimberg, F. Gel'mukhanov, M. N. Piancastelli, and M. Simon, Phys. Chem. Chem. Phys. **24**, 5842 (2022).
[28] A. G. Kochur, V. L. Sukhorukov, A. J. Dudenko, and P. V. Demekhin, J. Phys. B: At. Mol. Opt. Phys. **28**, 387 (1995).
[29] M. N. Mirakhmedov and E. S. Parilis, J. Phys. B: At. Mol. Opt. Phys. **21**, 795 (1988).
[30] A. P. Chaynikov, A. G. Kochur, A. I. Dudenko, I. D. Petrov, and V. A. Yavna, Phys. Scr. **98**, 025406 (2023).
[31] F. von Busch, U. Kuetgens, J. Doppelfeld, and S. Fritzsche, Phys. Rev. A **59**, 2030 (1999).
[32] S.-M. Huttula, P. Lablanquie, L. Andric, J. Palaudoux, M. Huttula, S. Sheinerman, E. Shigemasa, Y. Hikosaka, K. Ito, and F. Penent, Phys. Rev. Lett. **110**, 113002 (2013).
[33] O. Travnikova, T. Marchenko, G. Goldsztejn, K. Jänkälä, N. Sisourat, S. Carniato, R. Guillemin, L. Journel, D. Céolin, R. Püttner, H. Iwayama, E. Shigemasa, M. N. Piancastelli, and M. Simon, Phys. Rev. Lett. **116**, 213001 (2016).
[34] O. Travnikova, N. Sisourat, T. Marchenko, G. Goldsztejn, R. Guillemin, L. Journel, D. Céolin, I. Ismail, A. F. Lago, R. Püttner, M. N. Piancastelli, and M. Simon, Phys. Rev. Lett. **118**, 213001 (2017).
[35] J.-P. Rueff, J. M. Ablett, D. Céolin, D. Prieur, T. Moreno, V. Balédent, B. Lassalle-Kaiser, J. E. Rault, M. Simon, and A. Shukla, J. Synchrotron Radiat. **22**, 175 (2015).
[36] D. Céolin, J. M. Ablett, D. Prieur, T. Moreno, J.-P. Rueff, T. Marchenko, L. Journel, R. Guillemin, B. Pilette, T. Marin, and M. Simon, J. Electron Spectrosc. Relat. Phenom. **190**, 188 (2013).
[37] M. F. Gu, Can. J. Phys. **86**, 675 (2008).
[38] K. G. Dyall, I. P. Grant, C. T. Johnson, F. A. Parpia, and E. P. Plummer, Comput. Phys. Commun. **55**, 425 (1989).
[39] L. Asplund, P. Kelfve, B. Blomster, H. Siegbahn, and K. Siegbahn, Phys. Scr. **16**, 268 (1977).
[40] C. Nicolas and C. Miron, J. Electron Spectrosc. Relat. Phenom. **185**, 267 (2012).
[41] S. Kučas and V. Jonauskas, Phys. Rev. A **108**, 022810 (2023).
[42] A. Chaynikov, A. Kochur, and A. Dudenko, J. Electron Spectrosc. Relat. Phenom. **279**, 147522 (2025).
[43] F. Gelmukhanov and H. Ågren, Phys. Rev. A **54**, 379 (1996).
[44] M. Simon, L. Journel, R. Guillemin, W. C. Stolte, I. Minkov, F. Gel'mukhanov, P. Sałek, H. Ågren, S. Carniato, R. Taïeb, A. C. Hudson, and D. W. Lindle, Phys. Rev. A **73**, 020706(R) (2006).
[45] H.-J. Werner, P. J. Knowles, G. Knizia, F. R. Manby, and M. Schütz, WIREs Comput. Mol. Sci. **2**, 242 (2012).
[46] T. H. Dunning, J. Chem. Phys. **90**, 1007 (1989).
[47] D. E. Woon and T. H. Dunning, J. Chem. Phys. **98**, 1358 (1993).
[48] M. Reiher and A. Wolf, J. Chem. Phys. **121**, 2037 (2004).
[49] M. Reiher and A. Wolf, J. Chem. Phys. **121**, 10945 (2004).
[50] A. Wolf, M. Reiher, and B. A. Hess, J. Chem. Phys. **117**, 9215 (2002).